eTransportation 26 (2025) 100507

Contents lists available at ScienceDirect

eTransportation

journal homepage: www.journals.elsevier.com/etransportation

Design parameter optimization for sulfide-based all-solid-state batteries with high energy density

Jiyoung Kim [a,b], Charles Mish [b], Alexandre T.R. Guibert [b], Filippo Agnelli [b], Marta Vicencio [c], So-Yeon Ham [c], Min-Sang Song [a], Ying Shirley Meng [c,d], Jeong Beom Lee [a,c,*], H. Alicia Kim [b]

[a] LG Energy Solution, LG Science Park, Magokjungang 10-ro, Seoul, 07796, Republic of Korea
[b] Structural Engineering, University of California San Diego, La Jolla, CA, 92093, USA
[c] Materials Science and Engineering, University of California San Diego, La Jolla, CA, 92093, USA
[d] Pritzker School of Molecular Engineering, University of Chicago, Chicago, IL, 60637, USA

ARTICLE INFO

Keywords:
All-solid-state batteries
Sulfide solid electrolyte
Argyrodite
P2D model
Sensitivity
Design optimization

ABSTRACT

Sulfide-based all-solid-state batteries (ASSBs) are promising candidates for applications requiring high energy density and enhanced safety, with the potential to replace conventional Li-ion batteries. Despite significant advances in material design and engineering, the impact of material properties and process variables on cell energy density remains poorly understood. In this study, we employed a validated pseudo-two-dimensional (P2D) model to investigate how volumetric and gravimetric energy densities of ASSBs change as function of various cell design parameters and to perform mathematical optimization to maximize energy densities. Model parameters were derived from pellet cell experiments, incorporating a cathode composite with high-capacity NCM811 and densely packed fine argyrodite, alongside a bulk solid electrolyte separator with high ionic conductivity. The model's accuracy was confirmed by comparing simulation results with experimental voltage profiles, resulting in a root mean square error of 0.028 mV and an energy discrepancy of 0.7 %. Using the validated P2D model, we set energy densities as objective functions and scaled the pellet cell structure to automotive pouch cell dimensions to assess practical energy densities. A comprehensive sensitivity study was conducted on design parameters within the solid electrolyte separator and cathode composite. The weight percentage of the cathode active material was identified as a highly sensitive parameter, with other cathode composite parameters showing strong dependence on it. Employing a gradient-free direct search optimization method, we identified optimal design parameters that improved the volumetric and gravimetric energy densities by 62.5 % and 66.3 %, respectively, relative to reference values based on experimental parameters for a single cell.

1. Introduction

Sulfide-based all-solid-state batteries (ASSBs) hold significant promise for achieving high energy density, leveraging the excellent electrochemical stability of sulfide solid electrolyte (SEs) when paired with layered metal oxide cathode active material (CAM) and high-capacity anodes like lithium metal and anodeless configurations [1–3]. Extensive research has been dedicated to material engineering aimed at enhancing electrochemical properties in sulfide-based ASSBs. Chemically stable SEs with enhanced ionic conductivity, comparable to that of liquid electrolytes, have been developed for facilitating Li-ion conduction [4–9]. In the cathode composite, modifying the size and morphology of the active material has been shown to increase physical contact between the CAM and SE [10–12], and protective layers has been explored to reduce interfacial resistance [13–16]. In the anode, efforts to develop protective layers aim to suppress interfacial reactions and dendrite growth between Li metal and the SE separator [17–20].

Alongside these material advancements, research in electrode design has explored developing methods to reduce SE separator thickness [21–23] and modifying the particle sizes and composition of the active material and SE to improve cell performance [24,25]. Comprehensive experimental efforts are essential for identifying optimal designs for high energy density, but they can be time-consuming and resource intensive. To complement these experimental approaches and accelerate

* Corresponding author. LG Energy Solution, LG Science Park, Magokjungang 10-ro, Seoul, 07796, Republic of Korea.
E-mail address: jaybilee@lgensol.com (J.B. Lee).

https://doi.org/10.1016/j.etran.2025.100507
Received 1 August 2025; Received in revised form 2 October 2025; Accepted 27 October 2025
Available online 31 October 2025

the development process, computer-aided modeling offers a more efficient tool. In solid-state battery modeling, studies have focused on understanding the electrode behavior by investigating design parameters such as material properties, composition, and geometric properties of the electrode. Cistjakov et al. [26] modeled the impact of the core-shell cathode particle structure on cell performance in a polymer-based electrolyte system, while Shi et al. [27] examined how the particle size ratio between the CAM and SE affects cathode utilization. Bielefeld et al. [28,29] provided insights into electrode design by modeling factors such as particle size distribution, active material content, and porosity, which influence percolation, using a 3D microstructure framework.

Insights gained into each parameter within the electrode through modeling can be further applied to predict the cell's electrochemical performance [30–33]. The underlying physical and chemical processes occurring within a cell can be described as the charge and mass transport, in addition to lithiation of active particles. In particular, the pseudo-two-dimensional (P2D) model [34,35], a high-fidelity model recognized for its predictive accuracy in cell performance, is widely used in Li-ion batteries (LiBs). Wolff et al. [30] adapted the P2D model from a liquid electrolyte system to an SE system, incorporating the properties of a single ion conducting electrolyte. Their model was then used to elucidate differences in electrochemical performance between LiBs and ASSBs. The P2D model has also been applied to investigate cell performance under varying mass ratios of active material to SE in the graphite anode [31], as well as different sulfide SE particle sizes [32,33]. Furthermore, in LiBs, the P2D model has also been integrated into sensitivity analysis and optimization, offering a cost and time-efficient way to provide guidance on the optimal parameter values [36–42]. In polymer and oxide-based all-solid-state Li batteries [43], the P2D model was used to identify optimal combinations of polymer and oxide SEs, followed by global sensitivity analysis to evaluate design parameters affecting energy density. Subsequently, cathode thickness and the volume fraction of active materials were optimized to achieve the maximum energy density for the selected SE combinations. Despite the superior ionic conductivity, ductile mechanical behavior, and pressure processability of sulfide SEs, which make them highly promising for scalable production, previous studies have not applied P2D modeling to systematic sensitivity and optimization analyses. Our study addresses this gap by focusing exclusively on sulfide-based ASSBs and employing a modeling framework specifically tailored to the unique properties of sulfide SEs. This framework establishes quantitative links between material and process parameters and their combined impact on energy density. By integrating experimental validation, interdependency analysis, and multi-objective optimization, our work differs in both methodology and analytical scope, thereby providing a distinct and complementary contribution to the literature and offering practical guidance for the design of high energy density sulfide-based ASSBs.

The contributions of this study to the design of next-generation high-energy batteries are as follows.

1. Integration of experimental parameters into the P2D model: Using high-capacity NCM811 as the CAM, densely packed fine argyrodite in the cathode composite, and a bulk argyrodite separator, with two distinct sulfide electrolytes of different particle sizes and ionic conductivities.
2. Sensitivity analysis of design parameters: Focusing on the interdependence between CAM proportion and other influential factors to clarify their collective impact on energy density.
3. Optimization framework for practical applications: Developing a gradient-free direct search method based on a weighted sum of volumetric and gravimetric energy densities to determine optimal parameters, including the scaling of pellet cell structures to automotive pouch cell dimensions [44].

By uniting modeling with experimental validation, the study not only captures the relationships among material and process parameters but also establishes a methodological basis for designing optimized sulfide-based ASSBs. The schematic overview of this workflow is presented in Fig. 1.

2. Experiment

In this section, we describe the experimental procedures used to obtain physical and electrochemical parameters and to validate the modeling framework. First, the ionic conductivity of sulfide-based SEs was measured. Next, cathode composites were fabricated, and their ionic/electronic conductivity and tortuosity were evaluated to clarify transport characteristics within the composite structure. Finally, cathode half-cells were assembled and characterized to assess electrochemical performance.

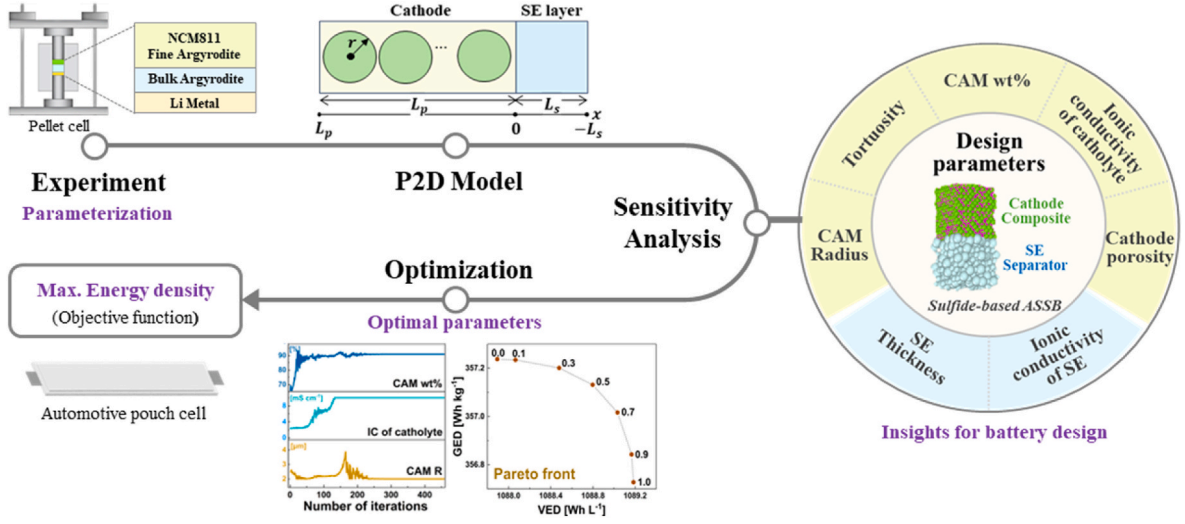

Fig. 1. Schematic overview of the work, from experimental parameterization and P2D modeling to sensitivity investigation of design parameters and optimization towards maximized energy density.

2.1. Solid electrolyte ionic conductivity measurements

We utilized two SEs of different particle sizes in pellet cell, as depicted in Fig. S1(a). The fine argyrodite (<1 μm, Mitsui) was incorporated into the cathode composite, while the bulk argyrodite (3 μm, Mitsui) was used in the SE separator. To measure the ionic and electronic conductivities of these SEs, SE pellets (50 mg) were prepared in a polyether ether ketone (PEEK) holder with a 10 mm diameter and two titanium plungers, followed by pressing at 375 MPa with a hydraulic press (Carver). Electrochemical Impedance Spectroscopy (EIS) measurements were performed under 75 MPa of uniaxial pressure from 7 MHz to 0.5 Hz with an applied potential of 10 mV using a Bio-Logic VSP-300. The results, presented in Fig. S1(b), were fitted with Z-View software.

2.2. Cathode composite fabrication and measurement of ionic/electronic conductivity, and tortuosity measurements

Fine argyrodite was employed as the catholyte for the cathode composite, with lithium zirconium oxide-coated lithium nickel cobalt manganese oxide (NCM811, LG Energy Solution) serving as the CAM and vapor-grown carbon fiber (VGCF, Sigma) as the conductive additive. The cathode composite was prepared by hand-mixing these components in weight ratios of NCM811: argyrodite: VGCF = 66:31:3, 75:22:3, and 85:12:3. For measurement of electronic conductivity, 50 mg of the cathode composite was pressed within the PEEK holder at 375 MPa using a hydraulic press. DC polarizations were obtained by applying 0.05 V, 0.1 V and 0.2 V bias potentials for 1 min using a Bio-Logic VSP-300, as shown in Fig. S1(c). For the ionic conductivity, the same amount of the cathode composite was placed between bulk argyrodite pellets. Then, $Li_{0.5}In$ alloy powder was placed on both sides of the argyrodite. As depicted in Fig. S1(d), EIS measurements were performed from 7 MHz to 0.5 Hz with an applied potential of 10 mV using the same equipment. Both the ionic and electronic conductivity measurements were evaluated under 75 MPa of uniaxial pressure. The ionic tortuosity (τ) of the cathode composite was calculated using the measured effective ionic conductivity (κ_{eff}) and volume fraction of SE (ε_e) in the composite, based on the relation $\kappa_{eff} = \kappa\frac{\varepsilon_e}{\tau}$ [43].

2.3. Cathode half-cell fabrication and characterization

For the cathode half-cells, 75 mg of bulk argyrodite was placed into the PEEK holder and compressed between two titanium rods at 120 MPa. The thickness of the SE separator was measured using a vernier caliper. Subsequently, 22.7 mg of the cathode composite with a composition of NCM811: argyrodite: VGCF = 66:31:3 was pressed at 375 MPa onto one side of the SE pellet. Then, 50 mg of $Li_{0.5}In$ alloy powder was added and pressed at 120 MPa on the opposite side of the SE pellet. The cell was secured into a cell holder under a pressure at 75 MPa and cycled over a voltage range of 4.3–3.0 V (vs Li/Li^+). For the measurement of capacity and voltage profile at various C-rates, the cycling rate was set to 0.1C (20 mA g^{-1}) for the first two cycles, and subsequently to 0.2C and 0.3C, with a constant voltage cut-off of 0.05C at the end of charging using a Neware Battery cycler. The stoichiometry of NCM811 was derived from the charge/discharge voltage profiles under conditions of 0.1C, ranging from 3.0 to 4.3 V, in constant current/constant voltage (CC/CV) mode plotted, as presented in Fig. S2(a). Additionally, the galvanostatic intermittent titration technique (GITT) was utilized to determine the open circuit voltage (OCV) and the Li-ion diffusion coefficient of the active material, as illustrated in Fig. S2(b). The GITT measurements were performed by applying a constant current pulse at 0.1C (20 mA g^{-1}) for 12 min, followed by an open-circuit relaxation period of 1 h to allow the active material to reach the equilibrium. This sequence was repeated over the discharge to obtain the transient voltage response at different states of charge (SOC). The Li-ion diffusion coefficient was estimated based on Fick's second law [45,46]. To prevent exposure to air, all electrochemical experiments were conducted in a glovebox filled with argon gas at 25 °C.

3. Model description

This section presents the P2D model governing equations and parameters used to simulate the electrochemical behavior of sulfide-based ASSBs, along with the methodology for sensitivity analysis and design optimization.

3.1. P2D model for sulfide-based ASSBs

We adapted the P2D model from Toghyani et al. [43] to simulate the cell performance of sulfide-based half-cell ASSBs. The P2D model is governed by the conservation laws for charge and mass of lithium ion in both the electrode and electrolyte, as described by Equations (1) – (6) in Table 1. These laws are coupled with the electrochemical reaction occurring at the interface between the electrode and electrolyte. This charge-transfer reaction, which involve Li-ion intercalation and deintercalation into the active material, is governed by the Butler–Volmer equation in Equation (7). The total current density includes both Faradaic current from the charge-transfer reactions and non-Faradaic current from the electric double layer, as shown in Equation (10). In ASSBs, differences in electrochemical potentials at the interface between the CAM and SE generate a space charge layer (SCL), which in turn leads to

Table 1
Governing equation including boundary conditions of the P2D model in ASSBs.

		Governing equations		Boundary conditions
Charge conservation	Electrolyte	$i_e = -\kappa_{eff}\nabla\phi_e,\ \nabla\cdot i_e = aj$	(1)	$\phi_e\vert_{x=-L_s} = 0,\ i_e\vert_{x=L_p} = 0$
		$\kappa_{eff} = \kappa\,\varepsilon_e^{\beta},\ a = 3\frac{\varepsilon_s}{R_c}$	(2)	
	Solid phase	$i = -\sigma_{s,eff}\nabla\phi,\ \nabla\cdot i = -aj$	(3)	$i\vert_{x=0} = 0,\ i\vert_{x=L_p} = \frac{I_{app}}{A}$
		$\sigma_{s,eff} = \varepsilon_s\sigma_s$	(4)	
Mass conservation	Electrolyte	$\frac{\partial c_e}{\partial t} = 0$	(5)	
	Solid phase	$\frac{\partial c_s}{\partial t} + \frac{1}{r}\frac{\partial(r^2N_r)}{\partial r} = 0,\ N_r = -D_s\frac{\partial c_s}{\partial r}$	(6)	$\left.\frac{\partial c_s}{\partial r}\right\vert_{r=0} = 0,\ \left.\frac{\partial c_s}{\partial r}\right\vert_{r=R} = -\frac{j}{FD_s},\ c_s\vert_{t=0} = c_0$
Electrochemical reaction		$j_{Li} = \begin{cases} 0, & -L_s < x < 0 \\ 2j_0(c)\sinh\left(\frac{F}{2RT}(\phi-\phi_e-U(c))\right), & 0 < x < L_p \end{cases}$	(7)	
		$j_0 = kFC_e^{\alpha}(c_{s,max}-c_s)^{\alpha}c_s^{1-\alpha}$	(8)	
		$\eta = \phi - \phi_e - U(c)$	(9)	
Electrical double layer		$j = j_{Li} + j_{DL}$	(10)	
		$j_{DL} = C_{DL}\frac{\partial(\phi-\phi_e)}{\partial t}$	(11)	

the formation of interfacial capacitance. In modeling studies of ASSBs, this interfacial behavior is commonly expressed using the same mathematical equation as the double-layer capacitance, as expressed in Equation (11) [30,43]. When applying the P2D model to sulfide-based ASSBs, we assume full coverage between the CAM and SE, meaning the active material is entirely in contact with the SE, with no side reactions at the interface. Additionally, a lithium-ion transference number of one is considered in the SE. As a result, the concentration gradient can be discarded since Li^+ ions are the sole charge carrier across the crystal lattice, as indicated in Equation (5).

The parameters for our simulations are listed in Table 2. A distinctive aspect of our model is the two different SE in the cathode composite and in the SE separator. Each region of the cathode composite and the SE separator have different geometric structures, therefore different parameters, such as volume fraction of SE, porosity, and Bruggeman coefficient, were utilized in our simulation. The Bruggeman coefficient (β) was obtained from the experimental ionic tortuosity values, following the relation $\tau = \varepsilon_e^{1-\beta}$ [43]. The simulation of sulfide-based ASSBs using the P2D model was undertaken using the open-source battery simulation library *PyBaMM* [47], which relies upon the finite volume solver. The discretization yields a set of differential-algebraic equations, which are subsequently solved using CasADI solver [48].

Table 2
Parameters for the simulation in *PyBaMM*.

Parameters	symbol	unit	value
Density of positive particle	ρ_p	g cm^{-3}	4.66
Density of solid electrolyte	ρ_{SE}	g cm^{-3}	2.07
Density of Conductive material	ρ_{CM}	g cm^{-3}	2.00
Density of Aluminum foil	ρ_{Al}	g cm^{-3}	2.71
Density of Copper foil	ρ_{Cu}	g cm^{-3}	8.91
Density of Li metal	ρ_{Li}	g cm^{-3}	0.54
Density of Aluminum pouch	ρ_{Pouch}	g cm^{-3}	1.45
Radius of NCM811 particle	R_c	μm	2.5
Thickness of solid electrolyte separator	L_s	μm	565
Thickness of Aluminum foil	L_{Li}	μm	15
Thickness of Copper foil	L_{Cu}	μm	12
Thickness of Aluminum pouch [44]	L_{Pouch}	μm	144
Dimension of Aluminum pouch (width × length) [44]	A_{Pouch}	cm^2	9.8 × 53.5
Dimension of cathode electrode (width × length) [44]	$A_{cathode}$	cm^2	9.0 × 51.0
Number of stacks in the cell	N_s	–	20
Volume fraction of cathode active material	ε_s	–	0.42
Volume fraction of solid electrolyte	ε_e	–	0.44
Porosity in solid electrolyte separator	p_s	%	5.0
Porosity in cathode composite	p_c	%	9.17
Electrode cross-sectional area	A	m^2	7.85 • 10^{-5}
Electrolyte concentration	c_e	mol m^{-3}	6110
Initial solid concentration	c_s	mol m^{-3}	9380
Maximum solid concentration	$c_{s,max}$	mol m^{-3}	49700
Electronic conductivity of NMC811	σ_s	mS cm^{-1}	20.6
Ionic conductivity in solid electrolyte separator	κ_s	mS cm^{-1}	5.01
Ionic conductivity in catholyte composite	κ_c	mS cm^{-1}	2.31
Diffusion coefficient	D_s	m^2 s^{-1}	6.9 • 10^{-16}
Double layer capacitance [43]	C_{DL}	F m^{-2}	0.2
Transfer coefficients [49]	α	–	0.5
Bruggeman coefficient in solid electrolyte separator	β_s	–	1.0
Bruggeman coefficient in cathode composite	β_c	–	2.67
Areal capacity	AL	Ah cm^{-2}	0.007
Molecular weight of Li	MW_{Li}	g mol^{-1}	6.941
Temperature	T	K	298.15
Faraday constant	F	C mol^{-1}	96485
Gas constant	R	J mol^{-1} K^{-1}	8.314
Open circuit voltage (OCV)	$U(c)$	V	Table S1

3.2. Sensitivity and design optimization

For the investigation of sensitivity and design optimization of sulfide-based ASSBs, we aim to maximize the volumetric and gravimetric energy densities during discharge, serving as two different objective functions. The energy densities, both volumetric (E_v) and gravimetric (E_g), are given by,

$$E_v = \int_0^{t_{cut-off}} \frac{I_{dis} \cdot V(t)}{V_{cell}} dt \tag{12}$$

$$E_g = \int_0^{t_{cut-off}} \frac{I_{dis} \cdot V(t)}{M_{cell}} dt \tag{13}$$

where I_{dis} represents the discharge current, $V(t)$ denotes the cell voltage, and V_{cell} and M_{cell} correspond to the cell volume and mass, respectively. To simulate energy densities for practical applications, we base our calculations on the dimensions of the automotive pouch cell. This involves adjusting the electrode dimensions from the pellet cell to the pouch cell and applying the stack structure, while retaining the design parameter values from the pellet cell. To determine the pouch cell dimension, we used the measured data from reference [44], which provides the thickness of Aluminum (Al) pouch as well as the pouch and cathode electrode dimension. From these values, we calculated the cell volume (V_{cell}) and mass (M_{cell}), while the area of the cathode electrode was utilized to calculate the energy, $I_{dis} \cdot V(t)$. Additionally, we considered the cell thickness at SOC100 % by accounting for the increase in lithium thickness in the anode during charging. The details for these calculations are shown in Equations (S1) – (S3).

To investigate how the selected design variables influence the energy densities, one parameter is scanned within a range of interests while the other parameters are held constant, visualizing the partial derivatives. After carrying out the sensitivity study for each parameter, design optimization was performed to identify optimum values that maximize the objective function. The design parameters are optimized using the Nelder-Mead method [50,51] also known as the downhill simplex method, which is implemented in SciPy [52]. The method is a direct search technique commonly used for solving nonlinear optimization problems. One of its key advantages is that it does not require gradient information, which can be difficult to obtain for complex models such as the P2D model. Instead, the method relies on direct comparison of function evaluations. The Nelder-Mead method operates by creating a simplex, i.e., a convex envelope, in the n-dimensional space $\mathbb{R}^n$ spanned by the design variables. The simplex is formed by n+1 vertices, where each vertex corresponds to a point at which the objective function has been evaluated. The algorithm then performs various transformations on the simplex, such as expansion or reflection, based on further function evaluations. These transformations aim to maximize the objective function by iteratively adjusting the vertices until the simplex converges to a sufficiently small size. In this work, the algorithm is set to stop when the absolute change from one iteration to another for both the design variables and the objective function is less than 1×10^{-4}.

4. Results and discussion

In this study, we first compare the electrochemical performance results from the experiments and simulations at different C-rates to verify the P2D model for sulfide-based ASSBs using *PyBaMM*. Then, key design parameters, i.e. SE thickness, ionic conductivity of SE separator, CAM weight fraction (wt%), ionic conductivity of catholyte, porosity of cathode, and CAM radius are chosen to investigate their effects on volumetric and gravimetric energy densities. Subsequently, the optimal values of each design parameter are determined using a gradient-free direct search method to maximize the energy densities.

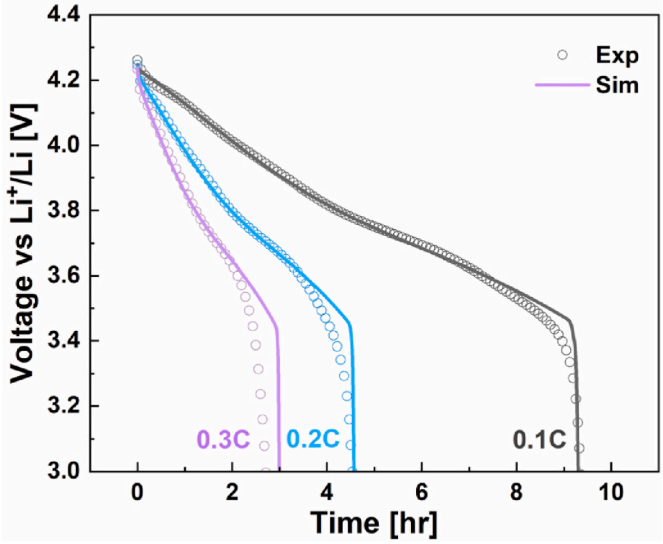

Fig. 2. Comparison of experimental and simulated voltage-time profiles for 0.1, 0.2, and 0.3C discharge at 25 °C.

4.1. Model validation

To validate our P2D model for sulfide-based ASSB, we compared experimental and simulated voltage-time profiles for discharge rates of 0.1C, 0.2C, and 0.3C at 25 °C (see in Fig. 2). The accuracy of the model was assessed using the Root Mean Square Error (RMSE), energy error, and discharge capacity error across the C-rates, as summarized in Table S2. All errors, including RMSE, capacity error, and energy error, exhibit a monotonic trend. While RMSE and energy error capture voltage deviations over the entire discharge profile, capacity error is determined solely by the capacity value at the cutoff voltage, making it more sensitive to local variations and experimental uncertainties near the end of discharge. The simulated voltages align with the experimental results across the three C-rates, both in the shape of the voltage profiles and in the discharge capacity at the cut-off voltage. Notably, the RMSE remained below 30 mV, the energy error stayed below 1.0 %, and the capacity error was kept under 3.5 % [53], which strongly supports the reliability of the model at 0.1C. As the C-rate increases, the RMSE deviations from the experimental results became more pronounced. This can be attributed to two simplifying assumptions in the model. Firstly, we assumed full coverage between active material and SE, where the ion transfer takes place over the entire surface of the active materials. In practice, however, the active materials are not fully covered with SEs due to their solid nature [54,55]. Secondly, our model did not include the influence of the Cathode Electrolyte Interphase (CEI) [56], a resistive layer formed by the oxidation of the electrolyte on the surface of active material, which can impede ionic transfer. We believe these two factors naturally lead to larger deviations at higher C-rates. Since the 0.1C result demonstrates the model's reliability, it will be used in our subsequent sensitivity and design optimization.

Table 3
Design parameters and the ranges.

Design parameters		Ref.	Lower	Upper
SE separator	SE ionic conductivity (mS cm^{-1})[a]	5.01	0.1	10
	SE layer thickness (μm)[b]	100	30	100
Cathode composite	CAM wt%[b]	66	66	93
	Catholyte ionic conductivity (mS cm^{-1})[a]	2.35	0.1	10
	Porosity (%)[b]	9.17	5	20
	CAM radius (μm)[a]	2.5	0.5	10

[a] Material property.
[b] Process variable.

4.2. Sensitivity to design parameters

The design parameters are classified into material properties and process variables for the SE separator and cathode composite, as shown in Table 3. The lower and upper limits for each parameter were selected based on the current technological constraints in materials and processes [57,58]. The reference values were chosen from the experimental data, with the exception of the SE separator thickness. Because the experimental thickness of 565 μm is not practical for high energy density cells, we reduced the SE separator thickness to 100 μm, which is the maximum value reported in review papers [59,60]. When this reduction was applied to our result at 0.1C, as shown in Fig. S3, the discharge profile remained consistent. This consistency is attributed to the assumption that the Li-ion concentration gradient in the SE separator was disregarded. In the sensitivity study, we examined the interdependency between design parameters while fixing the areal capacity to eliminate the influence of cell capacity variations caused by changes in CAM wt%.

Fig. 3 illustrates the variations in volumetric and gravimetric energy densities in response to the design parameters in Table 3. One component influencing energy densities is SE separator, which plays an important role in facilitating Li-ion transport between cathode and anode while preventing short circuits by blocking electron transfer. Given its role, understanding the impact of SE separator on cell performance is crucial for designing ASSBs. The sensitivity of energy densities to the SE separator thickness is evident in Fig. 3 (red curve). Reducing the SE thickness from 100 μm to 30 μm significantly decreases the cell volume and mass by 19.4 % and 12.3 %, respectively, while maintaining nearly constant energy output due to the consistent Li-ion concentration within the SE layer. This reduction in physical dimensions leads to a 24.2 % increase in the volumetric energy density and a 14.0 % increase in the gravimetric energy density. These results highlight the importance of reducing SE thickness to improve energy densities by directly influencing the cell's physical dimensions without sacrificing energy. Further reductions may enable even higher energy densities, but a thinner SE layer exposes to the risk of short circuits caused by defects, that are not captured in the P2D model. For this reason, we defined the minimal separator thickness based on three factors: (1) sufficient mechanical strength of SE separator films, (2) good slurry dispersibility and uniformity, and (3) reduced dendrite growth risk. Recent studies using various fabrication methods have produced thin, flexible SE layers with strong mechanics and stable performance [61–64]. The SE thicknesses reported in these studies typically ranged from 26 to 50 μm, with a 30

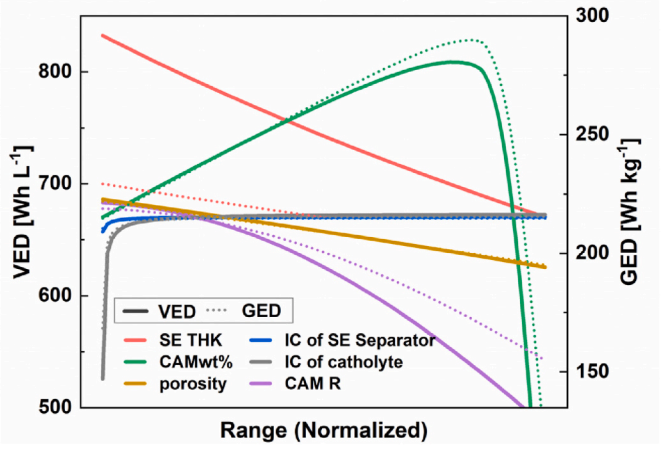

Fig. 3. Changes in volumetric (VED, line) and gravimetric (GED, dotted line) energy densities depending on design variables when normalized in the range of Table 3.

μm SE thickness observed in an ASSB with a Li metal anode, identical to the configuration used in our study [65].

In addition to the SE separator thickness, the SE ionic conductivity is an important factor, especially for battery systems operating at higher C-rates. As shown in Fig. 3 (blue curve), when the SE ionic conductivity falls below ~1.7 mS cm^{-1}, energy densities drop significantly. This effect becomes even more pronounced at higher C-rates, in Fig. S4, in which the normalized energy densities indicate that the threshold for SE ionic conductivity increases from 1.7 mS cm^{-1} at 0.1C to 2.9 mS cm^{-1} at 0.2C and 3.8 mS cm^{-1} at 0.3C. These results suggest that ensuring the SE's ionic conductivity surpasses the threshold suited to the battery's desired C-rate conditions is key for stable performance. However, at higher C-rates, additional considerations are required because two assumptions in our model, full coverage between the CAM and SE and the neglected CEI layer, can significantly affect cell performance. In practice, interfacial voids are inevitable, even though external pressure during fabrication can improve contact between rigid CAM particles and ductile SE particles. Limited coverage restricts Li-ion diffusion into particle interiors and increases overpotentials, effects that become more pronounced at higher C-rates [66]. In addition, a CEI layer, which forms from side reactions between the cathode surface and the SE, can also degrade cell performance at higher C-rates. To extend this work to higher C-rates, these assumptions should be revised and incorporated into the model.

We now examine the sensitivity to design parameters in the cathode composite. The design of the cathode composite is important in determining key battery performance metrics, including quick charging capability, power density, and energy density. The cathode design is particularly crucial in ASSBs, where the cathode composite incorporates solid catholytes to facilitate Li-ion transport. Although catholytes are essential for ion transport, increasing the catholyte fraction reduces the proportion of active material within a fixed volume, resulting in a trade-off between achieving high energy density and ensuring sufficient ionic percolation. Fig. 3 (green curve) shows that CAM wt% exhibits a distinctive increasing-then-decreasing trend, reaching the maximum volumetric and gravimetric energy densities at 87.2 and 88.5 wt%, respectively. To further investigate the effect of CAM wt%, we simulated voltage curves at CAM wt% ranging from 66 to 93 wt% at 0.1C, as seen in Fig. 4(a). Notably, the deviation of the discharge curves increases as CAM wt% rises, reflecting the higher overpotential caused by internal resistance, which lowers the cell voltage during discharge. The resulting increase in overpotential reduces the cell energy, defined by the area under the voltage curve, and once a certain threshold is exceeded, a sharp decline occurs, as shown in Fig. 4(b). At higher CAM wt%, this energy decline outweighs the benefits of reducing cell volume and mass, leading to the trend seen in Fig. 3 (green curve). A reason for the sharp increase in the overpotential is the reduced SE content in the cathode composite. Lowering the SE volume fraction markedly reduces effective ionic conductivity, as shown in Fig. 4(c), thereby restricting Li-ion transport pathways within the cathode composite. This increased transport resistance requires a larger extra voltage to sustain the reaction, manifesting as a higher overpotential during discharge. Based on these findings, it is evident that identifying optimal CAM wt% significantly influences ionic percolation within the cathode composite and is essential for maximizing energy densities.

Beyond the SE volume fraction, we study three other factors that influence effective ionic conductivity (IC). These are the IC of catholyte, the porosity, and the ionic tortuosity of the cathode composite. Through simulations, their influences on the volumetric and gravimetric energy densities, with considerations of the effect of CAM wt% are shown in Fig. 5. Fig. 5(a, dashed lines) shows the sensitivity of energy densities to the IC of catholyte, and the shape of the graph is similar to that of the SE separator's IC at 0.1C. However, at low IC (<1 mS cm^{-1}), the reduction in energy density is ~19.2 % greater for the catholyte's IC than for the SE separator's IC. At a higher C-rate (0.3C), while changes in the separator's IC have little effect on energy density above 0.5 mS cm^{-1}, the catholyte exhibits more significant variations in energy density within the range of 0.5–10 mS cm^{-1}. The higher sensitivity of catholyte's IC is attributed to the heterogeneity of the cathode composite, which creates more complex ionic pathways due to existence of CAM and conducting additives compared to the homogeneous SE separator. Fig. 5(b)–(d) present the simulated volumetric energy density and effective IC as a function of the catholyte's IC and CAM wt%. In Fig. 5(b), the sharp drop in the volumetric energy density at a certain CAM wt% arises from insufficient ionic conduction. However, increasing the catholyte' IC can shift this sudden decline to a higher CAM wt%. As illustrated in Fig. 5(c), at a given catholyte IC, raising the CAM wt% lowers the SE volume fraction, thereby reducing effective ionic conductivity. This loss in ionic conduction can be offset by using a higher catholyte IC to facilitate efficient Li-ion transfer within the cathode composite, as shown in Fig. 5 (d). When the CAM wt% exceeds 90.0 %, the required IC rises significantly, highlighting the importance of selecting an SE material that provides sufficient ionic pathways in the cathode composite. Since gravimetric energy density follows a trend similar to volumetric energy density, all results related to the design parameters affecting gravimetric energy density are shown in Fig. S5.

Cathode porosity depends on CAM wt%, which can be attributed to the higher elastic modulus of CAM particles compared with SEs [67,68], limiting their densification under applied pressure. In this work, however, porosity and CAM wt% were decoupled in the sensitivity analysis to independently quantify their effects on energy density, thereby providing clearer insight into their relative contributions. The results incorporating their interrelationship are presented in Figs. S6 and S7, showing that while the overall trend is preserved, VED decreases at higher CAM wt%. The range of porosity was determined based on current experiment considering the ductile property of sulfide SE and the previous studies on sulfide-based ASSBs conducted under fabrication pressures comparable to those used in our experiments [25,69,70]. The correlation between CAM wt% and porosity was obtained from experimental results and applied in the analysis, as illustrated in Fig. S8. Fig. 6

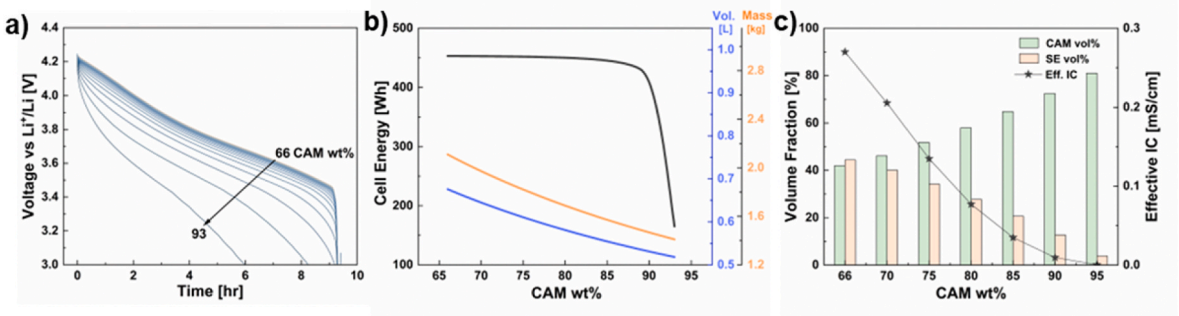

Fig. 4. (a) Simulated discharge voltage profiles for CAM wt% ranging from 66 % to 93 % in 1 % increments, (b) variation in energy, cell volume, and cell mass at various CAM wt%, (c) The change in CAM and SE volume fractions (vf) and effective ionic conductivity (IC) according to CAM wt%.

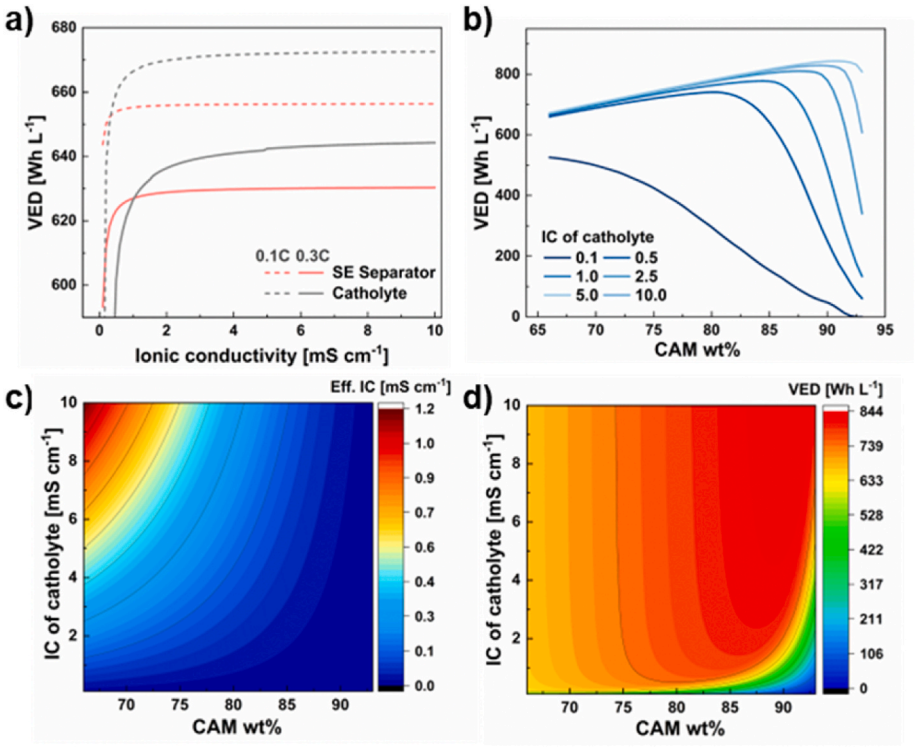

Fig. 5. (a) Volumetric energy density (VED) in relation to the IC of the SE separator and catholyte at 0.1C and 0.3C, (b) VED as a function of CAM wt% at catholyte ionic conductivity of 0.1, 0.5, 1.0, 2.5, 5.0, and 10.0 mS cm^{-1}, (c) contour plot showing the effect of CAM wt% and catholyte ionic conductivity on effective IC, (d) contour plot for the effect of CAM wt% and catholyte ionic conductivity on VED.

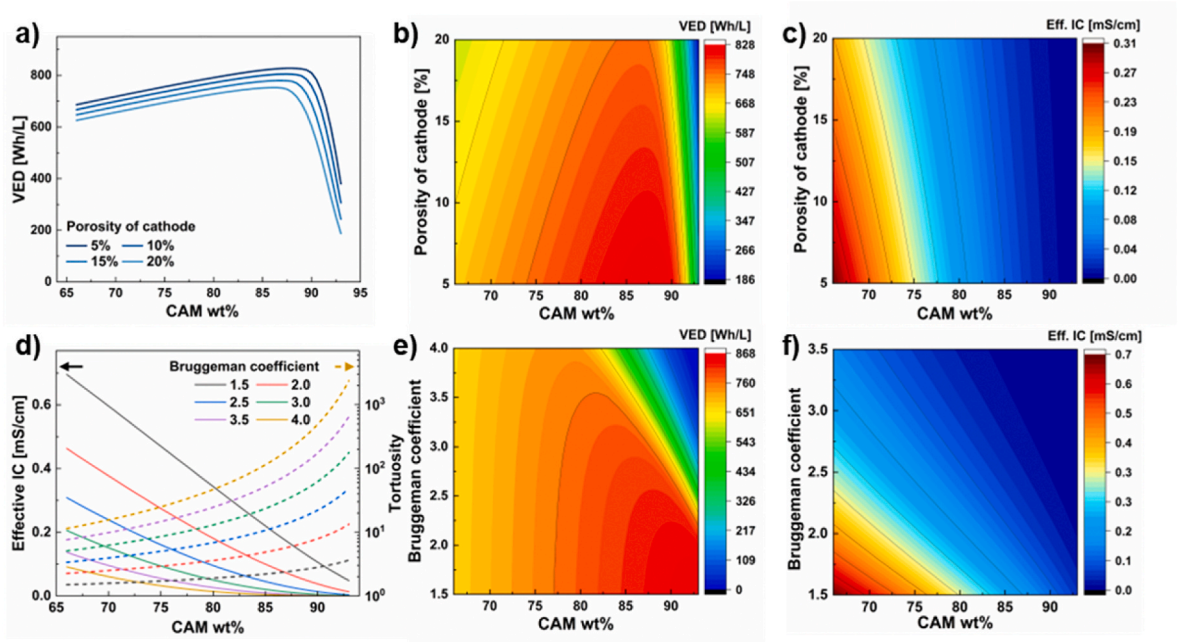

Fig. 6. (a) VED as a function of CAM wt% at cathode porosity of 5, 10, 15, 20 %, (b–c) contour plot illustrating the effect of CAM wt% and cathode porosity on VED and effective IC, respectively, (d) effective IC and ionic tortuosity for varying CAM wt% at different Bruggeman coefficient, ranging from 1.5 to 4.0, (e–f) contour plots showing the dependence of VED and effective IC on CAM wt% and Bruggeman coefficient.

(a) and **(b)** present the volumetric energy density across all CAM wt% ranges with cathode porosity treated as an independent variable. As porosity decrease, the energy density increases, because pores in the cathode obstruct ionic pathways and reduce the volume fraction of SE, limiting the effective ionic conductivity, as plotted in Fig. 6(c). Minimizing porosity enhances effective ionic conductivity, increase the volume fraction of active material, and reduces cathode thickness, thereby leading to higher volumetric energy density. To achieve this, especially at a higher CAM wt%, the fabrication process can be optimized by transitioning from uniaxial pressing to cold isostatic pressing

(CIP) or warm isostatic pressing (WIP), which are known to enable more dense cathode composite structures [71]. In this study, we examine the combined effects of cathode porosity and CAM wt% on volumetric energy density. However, porosity is also influenced by other factors, such as the size and size distribution of both CAM and SE particles [25,27,72,73], which affect overall cell performance. While these factors are not considered in the current simulation, incorporating them in future research could enable more accurate predictions of electrochemical behavior.

Next, we examine the impact of ionic tortuosity, which refers to the complexity of ion transport pathways through catholyte in the cathode composite, on the energy densities. The cathode composite in ASSBs is composed of a mixture of materials of varying sizes, including CAM, SE, carbon, and binder, along with pores. The degree of interconnection among the SE particles within the composite is crucial for ensuring sufficient ionic conduction, which determines the performance of the cathode. While ionic tortuosity cannot be directly controlled, it can be indirectly controlled by adjusting material particle sizes and optimizing the mixing and pressing processes. In this work, we utilized the Bruggeman coefficient to simulate the effect of ionic tortuosity on the energy densities. The Bruggeman relation, as shown in Equation (2), is used to calculate tortuosity in porous media with spherical particles in a homogeneous system. In LiBs, the Bruggeman coefficient has been widely employed to estimate effective IC, with a typical value of 1.5 [74–78]. In reality, CAM particles are not spherical, and a pore distribution is uneven, leading to deviations from the ideal ionic conduction pathway. As a result, the Bruggeman coefficient exceeds 1.5, indicating increased tortuosity in the actual microstructures. Fig. 6(d) shows the relationship between CAM wt% and effective IC by varying the Bruggeman coefficients from 1.5 to 4.0. As the Bruggeman coefficient increases, the slope of the effective ionic conductivity flattens, with a rapid decrease observed at a higher CAM wt%. Ionic tortuosity increases exponentially with rising Bruggeman coefficients and CAM wt%, indicating that the Li-ion pathways become more complex, thereby hindering ionic conduction. Fig. 6(e) and **(f)** illustrate that a lower Bruggeman coefficient leads to higher volumetric energy density and effective IC. The effective IC ranges from 0.01 to 0.27 mS cm^{-1} for energy densities above 800 Wh L^{-1}. Optimizing ionic tortuosity at high CAM wt% by modifying the shape and particle size of CAM and controlling fabrication pressure [79,80] can enhance ion transport pathways, leading to increased energy densities. Therefore, examining the factors that influence effective IC can guide the selection of SE materials and optimization of process conditions, helping to achieve target energy densities.

The sizes of CAM particles influence Li-ion diffusion within the particles and charge transfer at the interfacial CAM and catholyte. Reducing a CAM radius increases the overall interfacial surface area with the SE and decreases the Li-ion concentration on the surface of CAM particles during discharge [33]. Fig. 7(a) illustrates the simulated discharge voltage profiles for CAM radii ranging from 0.5 to 10 μm, showing that a larger CAM radius leads to a higher overpotential across the entire voltage range. During discharge, Li-ion concentration at the particle surface increases over time, as depicted in Fig. S9(a). At a given time, larger CAM radii result in higher surface concentrations due to the limited rate of Li-ion diffusion into the cathode particle. We simulate the Li-ion concentration from the cathode particle surface to the center to observe how the concentration gradient varies with CAM radius. In Fig. 7(b), the concentration remains uniform in the radial direction for a 1 μm particle, while the 10 μm particle exhibits noticeable variation within the particle. However, as shown in Fig. S9(b), the difference in the concentration gradient along the cathode thickness compared to the radial direction is minimal. An increasing CAM radius increases the diffusion path for Li-ions from the surface to the particle's center, leading to a higher concentration gradient. This gradient contributes to the overpotential and reduces both the capacity and the energy density. However, further reducing the CAM size does not result in higher energy density. As the CAM radius decrease, an increased surface area can significantly intensify side reactions at the CAM and SE interface [81]. Although side reaction is not accounted for in our simulation, Fig. S9(c) provides a preliminary guideline for selecting CAM radius of around 2 μm, where a sharp increase in surface area occurs. In future research, considering the impact of these side reactions could provide further insights into the optimal CAM size for achieving the maximum energy densities.

4.3. Mathematical optimization

The sensitivity investigation has provided valuable insights into how design parameter conflicts and influences the energy densities. We now apply a mathematical optimization method to identify the optimal balance of design parameters for maximum volumetric and gravimetric energy densities (VED and GED) within the parameter bounds in Table 3. We imposed constraints on the bounds of two design variables, CAM radius and cathode porosity. Since the model does not account for side reactions, we adjusted the lower limit of CAM radius to 2 μm, the point at which the surface area increases rapidly (see Fig. S6(c)). Additionally, while cathode porosity and CAM wt% were treated as independent parameters in the sensitivity study, in the optimization we consider cathode porosity as a dependent variable correlated with CAM wt%. To design a single cell with the maximum VED and GED, the multiobjective function is formulated using a weighted sum of both energy densities as below,

$$max.\ kE_v + (1-k)E_g \tag{14}$$

where k controls the weight between VED (E_v) and GED (E_g). Fig. 8

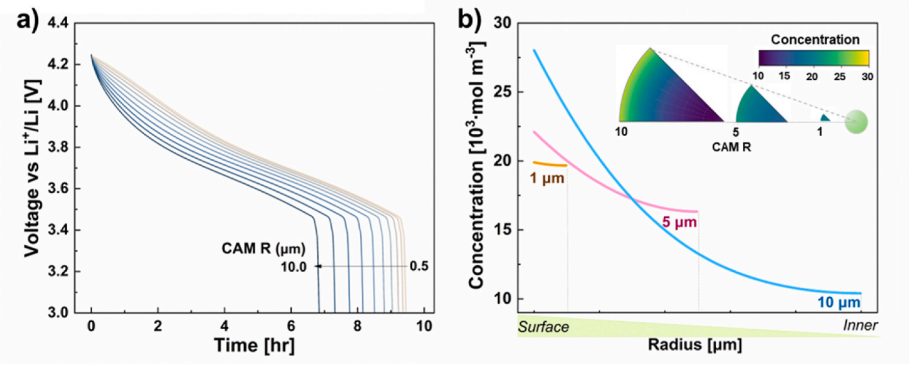

Fig. 7. (a) Simulated discharge voltage profiles for CAM radii (R) ranging from 0.5 to 10 μm and the simulations were conducted at R = 0.5 μm, and then from 1.0 to 10 μm in 1 μm increments, (b) Li-ion concentration from the cathode particle surface to the particle center for CAM radii of 1.0, 5.0, 10.0 μm at x = 50 μm, t = 3 h, with the concentration gradient in the radial direction of the particles shown in the inset.

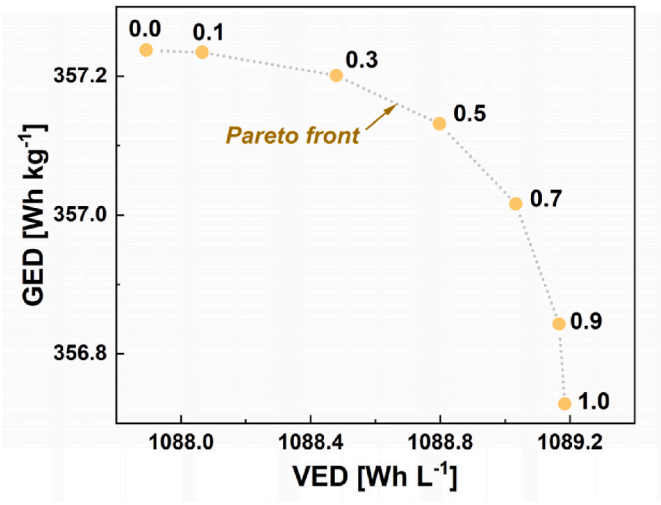

Fig. 8. Pareto front of optimal between VED and GED.

presents the Pareto front, where the curve represents the set of optimal VED and GED values based on the weighting factor (k). A higher k, indicating a greater emphasis on VED, shifts the optimal values toward higher VED. However, the overall differences between the volumetric and gravimetric energy densities are minimal, 1.2 Wh L^{-1} and 0.8 Wh kg^{-1}, respectively.

At $k = 0.5$, the optimized values of VED and GED are 1088.8 Wh L^{-1} and 357.1 Wh kg^{-1}, respectively, representing improvements of 62.5 % and 66.3 % relative to the reference values based on experimental parameters except that the SE separator thickness is set to 100 μm. These results are achieved when the CAM wt% is 91.0 % and cathode porosity is 14.3 %. The other design variables, including the SE separator thickness, the IC of the SE separator and catholyte, and CAM radius, reach their upper or lower bounds, as shown in Table 4 (Case 1). Although the optimization results indicate that these variables tend to approach their limits, our primary focus was on the CAM proportion. The CAM proportion directly affects other design factors in the cathode composite, such as porosity, tortuosity, and effective ionic conductivity, and our analysis quantitatively links these structural characteristics to electrochemical performance. This approach enabled us to determine, in a quantitative manner, the extent to which cathode content can be increased to maximize the energy density of ASSBs.

However, given the current stage of development, achieving an IC of 10 mS cm^{-1} is challenging. Therefore, we performed the optimization using the same constraint applied in the experiment, where the IC of the SE separator and catholyte were 5.01 and 2.31 mS cm^{-1}, respectively (Case 2). The obtained VED and GED are 1037.3 Wh L^{-1} and 335.5 Wh kg^{-1}, with a CAM content of 87.8 % and cathode porosity of 13.5 %. These results represent a reduction of 4.7 % in VED and 6.0 % in GED compared to the optimization using an IC of 10 mS cm^{-1}. The optimization results indicate that once the development of all materials and process is fully refined, high-energy density can be achieved even with a CAM portion as high as 90.0 %, provided that the SE has sufficient Li-ion conduction ability, optimal CAM size with ample interfacial contact area and minimal side reactions, and a thin SE separator. However, these findings were derived under modeled conditions using the dimensions of an automotive pouch cell currently applied in EVs. Although experimental validation is desirable to confirm the practical feasibility of the optimized design, the present stage of sulfide-based ASSB development still faces significant process and material-related challenges that hinder the fabrication of commercial scaled cells. While experimental validation of the optimized parameters was beyond the scope of this work, we consider it an essential direction for future research to verify the practical feasibility.

Table 4
Comparison of optimization results for Case 1 (optimal design) and Case 2 (design reflecting the current stage of SE's IC development).

	Case 1	Case 2
Volumetric energy density (Wh L^{-1})	1088.8	1037.3
Gravimetric energy density (Wh kg^{-1})	357.1	335.5
SE ionic conductivity (mS cm^{-1})	10.0	5.01
SE layer thickness (μm)	30	30
CAM wt%	91.0	87.8
Catholyte ionic conductivity (mS cm^{-1})	10.0	2.35
Cathode porosity (%)	14.3	13.5
CAM radius (μm)	2.0	2.0

5. Conclusions

This work presents a systematic framework for the design of sulfide-based ASSBs by integrating experimental parameterization, P2D modeling, sensitivity analysis, and optimization. The P2D model was validated against experimental voltage-time profiles, showing minimal deviation, and was subsequently employed to investigate the sensitivity of design parameters in both the SE separator and cathode composite. Sensitivity analysis revealed that minimizing separator thickness, while maintaining sufficient mechanical strength and high ionic conductivity, is essential for maximizing energy density. In the cathode composite, where CAM, SE, and pores form a complex structure, the CAM proportion plays a decisive role in shaping the ionic pathways of the SE. We therefore investigated how variations in CAM content interact with SE ionic conductivity, cathode porosity, and tortuosity to influence energy density. While higher CAM fractions enhance energy density by reducing inactive volume, excessive CAM loading decreases effective ionic conductivity and impedes ionic percolation. These effects were further clarified through analyses of catholyte conductivity, porosity, and tortuosity, which collectively govern ionic transport pathways. In addition, smaller CAM particle sizes were shown to improve interfacial contact and reduce overpotentials.

Building on these insights, a gradient-free optimization approach identified a high performance design with 91.0 % CAM wt% and 14.3 % cathode porosity, yielding volumetric and gravimetric energy densities of 1088.8 Wh L^{-1} and 357.1 Wh kg^{-1}, respectively, representing more than 60 % improvement over the reference design. Our simulations underscore that process optimization of the SE separator to reduce thickness while sustaining high ionic conductivity is essential, and that achieving high energy density in the cathode composite requires careful management of ionic transport limitations, microstructural effects, and interfacial properties. The present study assumes full coverage between CAM and SE and neglects CEI effects, both of which must be considered at high C-rates. Future work addressing these limitations and exploring the complex multivariate relationships among design parameters will provide more comprehensive insights and greater practical value for the optimized design of next-generation ASSBs.

CRediT authorship contribution statement

Jiyoung Kim: Writing – review & editing, Writing – original draft, Visualization, Validation, Software, Methodology, Investigation, Formal analysis, Data curation, Conceptualization. **Charles Mish:** Writing – review & editing, Visualization, Software, Methodology. **Alexandre T. R. Guibert:** Writing – review & editing, Software. **Filippo Agnelli:** Writing – review & editing. **Marta Vicencio:** Validation. **So-Yeon Ham:** Validation. **Min-Sang Song:** Resources. **Ying Shirley Meng:** Writing – review & editing, Funding acquisition. **Jeong Beom Lee:** Writing – review & editing, Validation, Methodology, Investigation, Conceptualization. **H. Alicia Kim:** Writing – review & editing, Supervision, Project administration, Funding acquisition, Conceptualization.

Declaration of competing interest

The authors declare that they have no known competing financial interests or personal relationships that could have appeared to influence the work reported in this paper.

Acknowledgement

This work was funded by the LG Energy Solution through Frontier Research Laboratory (FRL) program.

Appendix A. Supplementary data

Supplementary data to this article can be found online at https://doi.org/10.1016/j.etran.2025.100507.

Data availability

Data will be made available on request.

References

[1] Tan DHS, Meng YS, Jang J. Joule 2022;6:1755–69.
[2] Lee Y-G, Fujiki S, Jung C, Suzuki N, Yashiro N, Omoda R, Ko D-S, Shiratsuchi T, Sugimoto T, Ryu S, Ku JH, Watanabe T, Park Y, Aihara Y, Im D, Han IT. Nat Energy 2020;5:299–308.
[3] Ulissi U, Agostini M, Ito S, Aihara Y, Hassoun J. Solid State Ionics 2016;296:13–7.
[4] Jung WD, Jeon M, Shin SS, Kim JS, Jung HG, Kim BK, Lee JH, Chung YC, Kim H. ACS Omega 2020;5:26015–22.
[5] Lee Y, Jeong J, Lee HJ, Kim M, Han D, Kim H, Yuk JM, Nam K-W, Chung KY, Jung H-G, Yu S. ACS Energy Lett 2021;7:171–9.
[6] Huang B, Yao X, Huang Z, Guan Y, Jin Y, Xu X. J Power Sources 2015;284:206–11.
[7] Xu R-c, Xia X-h, Wang X-l, Xia Y, Tu J-p. J Mater Chem A 2017;5:2829–34.
[8] Xu R-c, Xia X-h, Li S-h, Zhang S-z, Wang X-l, Tu J-p. J Mater Chem A 2017;5:6310–7.
[9] Xie D, Chen S, Zhang Z, Ren J, Yao L, Wu L, Yao X, Xu X. J Power Sources 2018;389:140–7.
[10] Minnmann P, Strauss F, Bielefeld A, Ruess R, Adelhelm P, Burkhardt S, Dreyer SL, Trevisanello E, Ehrenberg H, Brezesinski T, Richter FH, Janek J. Adv Energy Mater 2022;12:2201425.
[11] Noh S, Nichols WT, Park C, Shin D. Ceram Int 2017;43:15952–8.
[12] Strauss F, Bartsch T, de Biasi L, Kim AY, Janek J, Hartmann P, Brezesinski T. ACS Energy Lett 2018;3:992–6.
[13] Culver SP, Koerver R, Zeier WG, Janek J. Adv Energy Mater 2019;9:1900626.
[14] Walther F, Strauss F, Wu X, Mogwitz B, Hertle J, Sann J, Rohnke M, Brezesinski T, Janek J. Chem Mater 2021;33:2110–25.
[15] Chen K, Yamamoto K, Orikasa Y, Uchiyama T, Ito Y, Yubuchi S, Hayashi A, Tatsumisago M, Nitta K, Uruga T, Uchimoto Y. Solid State Ionics 2018;327:150–6.
[16] Okada K, Machida N, Naito M, Shigematsu T, Ito S, Fujiki S, Nakano M, Aihara Y. Solid State Ionics 2014;255:120–7.
[17] Su H, Liu Y, Zhong Y, Li J, Wang X, Xia X, Gu C, Tu J. Nano Energy 2022;96:107104.
[18] Wang C, Adair KR, Liang J, Li X, Sun Y, Li X, Wang J, Sun Q, Zhao F, Lin X, Li R, Huang H, Zhang L, Yang R, Lu S, Sun X. Adv Funct Mater 2019;29:1900392.
[19] Xu R, Han F, Ji X, Fan X, Tu J, Wang C. Nano Energy 2018;53:958–66.
[20] Liang J, Li X, Zhao Y, Goncharova LV, Li W, Adair KR, Banis MN, Hu Y, Sham TK, Huang H, Zhang L, Zhao S, Lu S, Li R, Sun X. Adv Energy Mater 2019;9:1902125.
[21] Liu S, Zhou L, Han J, Wen K, Guan S, Xue C, Zhang Z, Xu B, Lin Y, Shen Y, Li L, Nan CW. Adv Energy Mater 2022;12:2200660.
[22] Tan DHS, Banerjee A, Deng Z, Wu EA, Nguyen H, Doux J-M, Wang X, Cheng J-h, Ong SP, Meng YS, Chen Z. ACS Appl Energy Mater 2019;2:6542–50.
[23] Kim DH, Lee Y-H, Song YB, Kwak H, Lee S-Y, Jung YS. ACS Energy Lett 2020;5:718–27.
[24] Kim YJ, Hoang TD, Han SC, Bang JA, Kang HW, Kim J, Park H, Park J-H, Park J-W, Park G, Lee Y-J, Kim D, Eom S-W, Choi J-H, Lee S-K, Moon J, Ha Y-C, Kim BG. Energy Storage Mater 2024;71:103607.
[25] Park C, Lee S, Kim K, Kim M, Choi S, Shin D. J Electrochem Soc 2019;166:A5318–22.
[26] Cistjakov W, Laue V, Röder F, Krewer U. J Electrochem Soc 2022;169:050510.
[27] Shi T, Tu Q, Tian Y, Xiao Y, Miara LJ, Kononova O, Ceder G. Adv Energy Mater 2019;10:1902881.
[28] Bielefeld A, Weber DA, Janek J. ACS Appl Mater Interfaces 2020;12:12821–33.
[29] Bielefeld A, Weber DA, Janek J. J Phys Chem C 2018;123:1626–34.
[30] Wolff N, Röder F, Krewer U. Electrochim Acta 2018;284:639–46.
[31] Park J, Kim D, Appiah WA, Song J, Bae KT, Lee KT, Oh J, Kim JY, Lee Y-G, Ryou M-H, Lee YM. Energy Storage Mater 2019;19:124–9.
[32] Scheller M, Durdel A, Frank A, Kriegler J, Jossen A. J Electrochem Soc 2024;171:020509.
[33] Iwamoto S, Kodama M, Yanagi K, Haniu Y, Fujii Y, Masuda N, Higuchi H, Suetsugu Y, Hirai S. J Power Sour Adv 2023;21:100120.
[34] Doyle M, Fuller TF, Newman J. J Electrochem Soc 1993;140:1526–33.
[35] Brosa Planella F, Ai W, Boyce AM, Ghosh A, Korotkin I, Sahu S, Sulzer V, Timms R, Tranter TG, Zyskin M, Cooper SJ, Edge JS, Foster JM, Marinescu M, Wu B, Richardson G. ProgressEnergy 2022;4:042003.
[36] Pan T-C, Liu E-J, Ku H-C, Hong C-W. Electrochim Acta 2022;404:139574.
[37] Lai Q, Jangra S, Ahn HJ, Kim G, Joe WT, Lin X. J Power Sources 2020;472:228338.
[38] Jokar A, Rajabloo B, Désilets M, Lacroix M. J Electrochem Soc 2016;163:A2876–86.
[39] Lagnoni M, Nicolella C, Bertei A. Electrochim Acta 2021;394:139098.
[40] Appiah WA, Busk J, Vegge T, Bhowmik A. Electrochim Acta 2023;439:141430.
[41] Shen X, Li X, Niu S, Du L. J Energy Storage 2024;101:113891.
[42] Wang Z, Zhou X, Zhang W, Sun B, Shi J, Huang Q. J Energy Storage 2023;68:107788.
[43] Toghyani S, Baakes F, Zhang N, Kühnelt H, Cistjakov W, Krewer U. J Electrochem Soc 2022;169:040550.
[44] Günter FJ, Wassiliadis N. J Electrochem Soc 2022;169:030515.
[45] Wen CJ, Boukamp BA, Huggins RA, Weppner W. J Electrochem Soc 1979;126:2258.
[46] Huggins WWaRA. J Electrochem Soc 1977;124:1569.
[47] Sulzer V, Marquis S, Timms R, Robinson M, Chapman S. J Open Res Software 2021;9.
[48] Andersson JAE, Gillis J, Horn G, Rawlings JB, Diehl M. Math Program Comput 2018;11:1–36.
[49] Legrand N, Raël S, Knosp B, Hinaje M, Desprez P, Lapicque F. J Power Sources 2014;251:370–8.
[50] Gao F, Han L. Comput Optim Appl 2010;51:259–77.
[51] Nelder JA, Mead R. Comput J 1965;7:308–13.
[52] Virtanen P, Gommers R, Oliphant TE, Haberland M, Reddy T, Cournapeau D, Burovski E, Peterson P, Weckesser W, Bright J, van der Walt SJ, Brett M, Wilson J, Millman KJ, Mayorov N, Nelson ARJ, Jones E, Kern R, Larson E, Carey CJ, Polat I, Feng Y, Moore EW, VanderPlas J, Laxalde D, Perktold J, Cimrman R, Henriksen I, Quintero EA, Harris CR, Archibald AM, Ribeiro AH, Pedregosa F, van Mulbregt P, SciPy C. Nat Methods 2020;17:261–72.
[53] Dessantis D, Di Prima P, Versaci D, Santarelli M, Bella F, Kolotygin V, López-Aranguren P, Amici J. Chem Eng J Adv 2024;18:100610.
[54] Hayakawa E, Nakamura H, Ohsaki S, Watano S. Adv Powder Technol 2022;33:103470.
[55] Koerver R, Aygün I, Leichtweiß T, Dietrich C, Zhang W, Binder JO, Hartmann P, Zeier WG, Janek J. Chem Mater 2017;29:5574–82.
[56] Zhang SS, Xu K, Jow TR. Electrochem Solid State Lett 2002;5:A92–4.
[57] Sung J, Heo J, Kim D-H, Jo S, Ha Y-C, Kim D, Ahn S, Park J-W. Mater Chem Front 2024;8:1861–87.
[58] Lee H, Oh P, Kim J, Cha H, Chae S, Lee S, Cho J. Adv Mater 2019;31:e1900376.
[59] Wu J, Yuan L, Zhang W, Li Z, Xie X, Huang Y. Energy Environ Sci 2021;14:12–36.
[60] Sang J, Tang B, Pan K, He Y-B, Zhou Z. Acc Mater Res 2023;4:472–83.
[61] Lee DJ, Jeon Y, Lee JP, Zhang L, Koh KH, Li F, Mu AU, Wu J, Chen YT, McNulty S, Tang W, Vicencio M, Xu D, Kim J, Chen Z. Nat Commun 2025;16:4200.
[62] Li D, Liu H, Wang C, Yan C, Zhang Q, Nan CW, Fan LZ. Adv Funct Mater 2024:34.
[63] Li R, Mao Y, Chen N, Liu Q, Shao J, Liao Z, Qiu K, Wang P, Hao S, Liao X, Wang H, Wei Y, Guo C, Liu X, Zhu G, Ren D, Lu L, Ouyang M. J Energy Storage 2025:106.
[64] Nam YJ, Oh DY, Jung SH, Jung YS. J Power Sources 2018;375:93–101.
[65] Zhang Z, Wu L, Zhou D, Weng W, Yao X. Nano Lett 2021;21:5233–9.
[66] Lee D, Shim Y, Kim Y, Kwon G, Choi SH, Kim K, Yoo DJ. Nat Commun 2024;15:4763.
[67] Koerver R, Zhang W, Biasi Ld, Schweidler S, Kondrakov AO, Kolling S, Brezesinski T, Hartmann P, Zeier WG, Janek J. Energy Environ Sci 2018;11:2142–58.
[68] Zhang F, Guo Y, Zhang L, Jia P, Liu X, Qiu P, Zhang H, Huang J. eTransportation 2023;15:100220.
[69] Doux J-M, Yang Y, Tan DHS, Nguyen H, Wu EA, Wang X, Banerjee A, Meng YS. J Mater Chem A 2020;8:5049–55.
[70] Doerrer C, Capone I, Narayanan S, Liu J, Grovenor CRM, Pasta M, Grant PS. ACS Appl Mater Interfaces 2021;13:37809–15.
[71] Dixit M, Beamer C, Amin R, Shipley J, Eklund R, Muralidharan N, Lindqvist L, Fritz A, Essehli R, Balasubramanian M, Belharouak I. ACS Energy Lett 2022;7:3936–46.
[72] Minnmann P, Schubert J, Kremer S, Rekers R, Burkhardt S, Ruess R, Bielefeld A, Richter FH, Janek J. J Electrochem Soc 2024;171.
[73] Schlautmann E, Weiß A, Maus O, Ketter L, Rana M, Puls S, Nickel V, Gabbey C, Hartnig C, Bielefeld A, Zeier WG. Adv Energy Mater 2023;13.
[74] Chen C-H, Brosa Planella F, O'Regan K, Gastol D, Widanage WD, Kendrick E. J Electrochem Soc 2020;167:080534.
[75] Xu L, Lin X, Xie Y, Hu X. Energy Storage Mater 2022;45:952–68.
[76] O'Regan K, Brosa Planella F, Widanage WD, Kendrick E. Electrochim Acta 2022;425:140700.
[77] Hosseinzadeh E, Marco J, Jennings P. Energies 2017;10:1278.
[78] Kim J, Mallarapu A, Santhanagopalan S, Newman J. J Power Sources 2023;556:232413.
[79] Park S-Y, Jeong J, Shin H-C. Appl Sci 2022;12:12692.
[80] Akbar A, Weng J, Zhang X, Li P, Ye G, Zhou X. Ind Eng Chem Res 2024;63:8971–82.
[81] Zhang J, Qiao J, Sun K, Wang Z. Particuology 2022;61:18–29.